NUMERICAL AND EXPERIMENTAL VALIDATION OF HOMOGENIZATION TECHNIQUES FOR BUBBLE DECK SLABS

Tomasz GARBOWSKI[1], Natalia STASZAK[2], Wojciech KOSTRZEWSKI[3],
Anna SZYMCZAK-GRACZYK[3*]

[1] Department of Biosystems Engineering, Poznan University of Life Sciences, Poland
[2] Doctoral School, Poznan University of Life Sciences, Poland
[3] Department of Construction and Geoengineering, Poznan University of Life Sciences, Poland

A b s t r a c t

This study investigates the deflection behaviour of Bubble Deck slabs using numerical and experimental approaches. Two techniques—numerical homogenization and 3D cross-sectional integration—are applied to derive equivalent properties for simplified finite element models. A scaled slab specimen (1020×2040×60 mm) with a reinforcement mesh of Ø4 bars spaced at 30 mm (top and bottom) and plastic spheres (Ø40 mm, spaced at 60 mm) is tested under self-weight and a mid-span linear load. The slab, simply supported on two shorter edges, is modelled both in full 3D and using simplified 2D model with homogenized parameters. Experimental deflections are compared with numerical and analytical/theoretical predictions to validate the proposed techniques, demonstrating their effectiveness in simplifying structural analyses while maintaining accuracy.

Keywords: Bubble Deck slab, numerical homogenization, 3D cross-section integration, deflection analysis, finite element method, structural validation

1. INRODUCTION

Prefabricated concrete structures such as floor slabs, girders, and columns have numerous advantages, including (a) quality standard, (b) saving of formwork, (c) short construction time, (d) durability of the structure, and (e) very low energy consumption [1-4]. These characteristics have made prefabricated concrete elements widely used in industrial and residential buildings worldwide over the past decades [2,5]. Among these, floor slabs and girders are some of the most frequently utilized prefabricated structural elements [5,6].

[3*] Corresponding author: Anna Szymczak-Graczyk, Poznan University of Life Sciences, Faculty of Environmental and Mechanical Engineering, Department of Construction and Geoengineering, Piątkowska Street 94, 60-649 Poznań, e-mail: anna.szymczak-graczyk@up.poznan.pl, phone: +48602516345

One of the most innovative prefabricated floor systems is the bubble deck ceiling. Originally designed in the late 1990s by Jorgen Bruenig, this system uses hollow plastic spheres to replace the non-structural concrete within slabs, significantly reducing the dead weight while maintaining two-way action [7-11]. The bubble deck ceiling consists of evenly distributed plastic inserts secured within a steel reinforcement cage, placed between the upper and lower reinforcement layers of a reinforced concrete slab [11-13]. Such systems align with both technical requirements, including strength, stiffness, and durability, and economic considerations such as reduced construction and operating costs [14,15,16,17]. By reducing the amount of concrete by up to 50% and using recyclable HDPE plastic, this approach also contributes to sustainable construction practices [10,11,18-20].

Despite these advantages, the analysis and optimization of bubble deck slabs present challenges due to their complex structure. Full three-dimensional finite element (FE) modelling is often required to accurately capture the mechanical behaviour of such systems under various loading conditions. Numerous studies have developed 3D models to simulate nonlinear behaviour and assess specific aspects like shear stress or bending performance [21-27]. While effective, such detailed modelling is computationally intensive and time-consuming, making it impractical for routine engineering tasks.

A promising alternative is homogenization, a mathematical technique that simplifies complex structures into models with equivalent properties. Homogenization enables engineers to replace multilayer composite cross-sections with single-layer models that retain equivalent mechanical behaviour. Various methods, including periodic homogenization [28,29], strain energy-based approaches [30,31], and multi-scale homogenization [32,33], have been proposed and extensively studied. Biancolini's method of strain energy equivalence [31] and its subsequent extensions [34,35] have proven particularly effective for analysing sandwich panels and composite structures.

In the context of bubble deck ceilings, numerical homogenization offers a viable solution for balancing computational efficiency with accuracy. By replacing the full 3D representative volume element (RVE) with a simplified shell model, this approach enables the analysis of large-scale systems while retaining the essential mechanical characteristics of the original structure [34-36]. Homogenization techniques have also been successfully applied to optimize bubble deck slab designs, minimizing concrete usage while ensuring compliance with serviceability limit states [35-38].

This paper focuses on validating two homogenization methods for bubble deck ceilings: numerical homogenization and spatial integration-based homogenization. The former uses finite element analysis to compute stiffness matrices of simplified models, while the latter integrates material properties over the RVE domain to derive effective parameters. Both methods are assessed against experimental data, including displacements and deflections under realistic loading conditions, to ensure their reliability and accuracy. The presented work builds upon previous studies [28,35-38] and introduces improvements to existing methodologies, particularly in accounting for transverse shear effects and optimizing bubble deck configurations.

The novelty of this research lies in its comprehensive validation framework, combining numerical and experimental techniques to evaluate the performance of bubble deck ceilings. By demonstrating the efficacy of homogenization methods in accurately predicting structural behaviour, this study contributes to advancing sustainable and efficient design practices in prefabricated concrete construction.

2. METHODS AND MATERIALS

2.1. Experimental model

The experimental model is a scaled-down slab designed for laboratory conditions, with dimensions of 2040 mm × 1020 mm and a thickness of 60 mm. The slab incorporates spherical voids created by

uniformly distributed ping-pong balls, arranged in a 34×17 grid across the slab's length and width. Each ball has a standard diameter of 40 mm. The slab is reinforced with a top and bottom mesh of Ø3 mm steel bars, spaced at 30 mm intervals. The concrete cover is 15 mm and bottom surfaces (Figure1a,1b,1c).

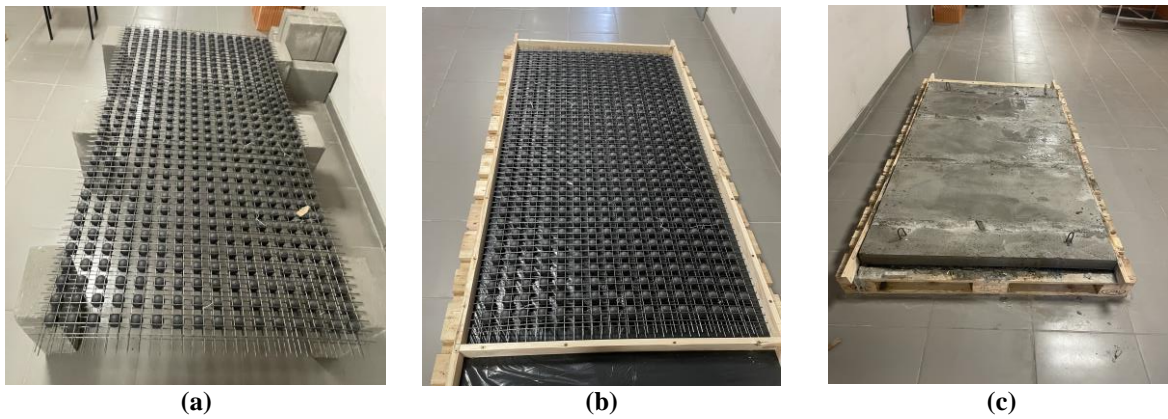| **(a)** | **(b)** | **(c)** |

Fig. 1. Bubble deck slab, **(a)** meshes of steel bars with balls between, **(b)** model of slab prepared for concreting, **(c)** concreted slab

The slab is simply supported along its shorter edges, with supports placed 20 mm from each edge. It is subjected to self-weight and a uniformly distributed line load applied along the middle of its span, across the entire width. The total applied load is approximately 500 kg, ensuring non-destructive testing while generating measurable deflections. Deflections are measured using a laser with an accuracy of 10 micrometres, enabling precise analysis of the slab's performance under load.

Table 1. Material properties

Material	**Young's Modulus (E)**	**Poisson's Ratio (ν)**	**Density (ρ)**
Concrete (C20/25)	25 GPa	0.2	2400 kg/m³
Steel (Reinforcement)	205 GPa	0.3	7850 kg/m³

In the following section, the volumes of concrete, voids, and reinforcement materials are calculated to accurately determine the self-weight of the slab. This is essential for ensuring that the experimental model reflects realistic loading conditions and provides reliable data for validating numerical simulations. To calculate the concrete volume, the total volume of the slab is reduced by the volume of the voids created by the ping-pong balls and the volume of the reinforcement steel mesh.

- Total slab volume: $V_{slab} = L \cdot W \cdot H = 0.124848 \, \text{m}^3$
- Volume of ping-pong balls:
  - Volume of one ball: $V_{ball} = \frac{4}{3}\pi r^3 = 3.351 \cdot 10^{-5} \, \text{m}^3$
  - Total volume of 34×17 balls: $V_{balls} = 34 \cdot 17 \cdot V_{ball} = 0.019369 \, \text{m}^3$
- Volume of steel mesh:
  - Volume of a bar per unit length: $V_{bar} = \pi r^2 \cdot L_{bar} = 0.707 \cdot 10^{-5} \, \text{m}^3$

- - Total bars (top and bottom mesh): Number of 2m long bars per mesh (top and bottom): $2 \cdot 33 = 66$ pcs; Number of 1m long bars per mesh (top and bottom): 132 pcs; $V_{steel} = 264 \cdot V_{bar} = 0.001866 \, \text{m}^3$
- Net concrete volume: $V_{concrete} = V_{slab} - V_{balls} - V_{steel} = 0.103613 \, \text{m}^3$

Summary:
- Total concrete weight: $0.1036 \, \text{m}^3 \cdot 2400 \, \text{kg/m}^3 = 248.67 \, \text{kg}$.
- Total weight reduction (balls): $0.0194 \, \text{m}^3 \cdot 2400 \, \text{kg/m}^3 = 46.48 \, \text{kg} \, (15,5\%)$.
- Reinforcement steel weight: $0.0019 \, \text{m}^3 \cdot 7850 \, \text{kg/m}^3 = 14.65 \, \text{kg}$.

2.2. Representative Volume Element (RVE)

A Representative Volume Element (RVE) is a fundamental building block used in computational mechanics to model materials with periodic structures or repetitive patterns. It captures the essential microstructural features of the material, such as voids, inclusions, or reinforcement elements, and is designed to represent the macroscopic behaviour of a material when subjected to external loads. The RVE is a critical component in homogenization techniques, which aim to bridge the gap between microscale and macroscale analysis.
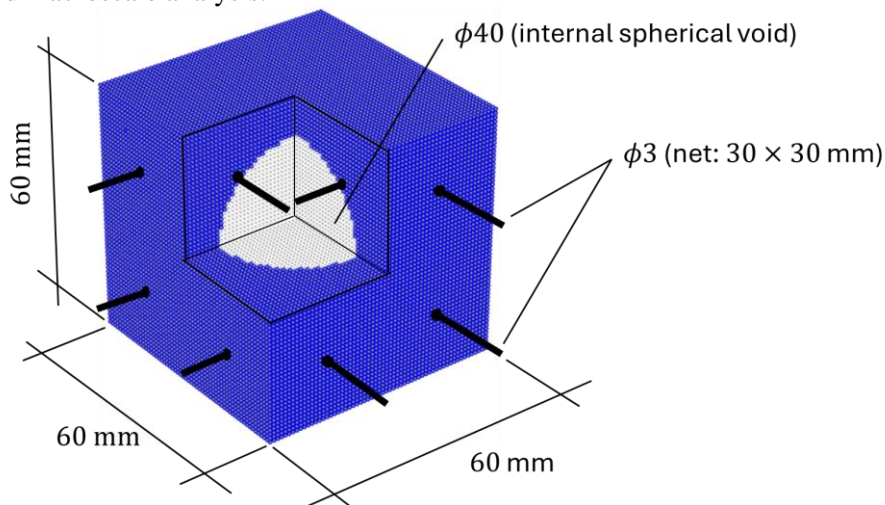

Fig. 2. Representative Volume Element (RVE) of the slab with spherical voids ($\phi = 40$ mm) and reinforcement bars ($\phi = 3$ mm)

Figure 2 illustrates the Representative Volume Element for the analysed structure. It is a highly detailed computational model that accurately replicates all the features of the real-world slab, including the spherical voids with a diameter of 40 mm and the reinforcement bars. The voids are symmetrically distributed within the volume, ensuring periodicity, which is a key characteristic of the RVE.

In this periodic and condensed model, the geometry and material properties are discretized using nodes or finite elements to capture the detailed interactions between the voids, reinforcement, and surrounding concrete. The RVE includes a mesh of nodes or finite elements that accurately represents the spherical void, enabling precise analysis of the mechanical response of the structure. Such detailed modelling ensures that both analytical integrals and the condensed stiffness matrix derived from the RVE can reliably reflect the global behaviour of the entire slab.

This periodic and condensed approach leverages homogenization techniques, simplifying the complexity of analysing the full-scale slab while retaining the accuracy needed to study its structural

performance. The RVE serves as the foundational unit for understanding the interplay between microstructural features and macroscopic mechanical properties.

There are two main approaches to homogenization, described in details later in this article First uses spatial integration of RVE. This approach analytically integrates material properties across the RVE domain. It discretizes the RVE into infinitesimally small regions and performs integration to calculate effective material parameters such as stiffness or compliance. One major advantage is that the size of the elements in the RVE can be extremely small, ensuring high accuracy without computationally expensive matrix operations. Unlike numerical methods, this approach does not require solving large systems of equations, making it computationally efficient.

The other one - Numerical Homogenization based on Finite Elements (FE) involves meshing the RVE with finite elements and solving the resulting stiffness matrix numerically. While this approach allows for detailed discretization within the RVE, it comes with significant computational challenges. The stiffness matrix for a finely discretized RVE can contain tens or hundreds of thousands of rows and columns, requiring substantial computational resources for operations such as matrix inversion, which is standard in static condensation. For example, in a detailed model, the inversion of large stiffness matrices becomes a bottleneck, limiting the scalability of the approach for highly detailed or large-scale RVEs.

While numerical homogenization is highly versatile, its computational intensity imposes practical limits. The need to generate and manipulate large matrices makes it unsuitable for problems requiring extreme resolution or a high degree of precision in the discretization. Additionally, memory requirements and computation time grow exponentially with the size of the RVE, further emphasizing the importance of selecting an appropriate balance between accuracy and computational cost.

Despite these limitations, RVEs remain an invaluable tool in material modelling and design. Advances in computational power and algorithms are continuously improving the feasibility of numerical homogenization for larger and more complex problems. Hybrid approaches that combine numerical and analytical homogenization may provide a pathway to leverage the strengths of both methods, balancing computational efficiency with accuracy. In the case of models with periodic microstructures like the one shown, RVEs provide a robust framework for studying the interplay between microstructural geometry and macroscopic behaviour, offering insights that guide material optimization and structural design.

2.3.   Numerical homogenization

In homogenization, the goal is to transform a complex 3D model into a simplified 2D representation that, through effective parameters, accurately reflects the behaviour of the full 3D model. This approach is particularly effective for calculating displacements with high precision. Numerical homogenization leverages a numerical model based on the finite element method (FEM) without the need to solve the full system of equations. Instead, only the stiffness matrix of the Representative Volume Element (RVE) and the displacement-strain transformation matrix are required.

The following steps outline the key procedures for calculating the effective (equivalent) stiffness of a Bubble Deck slab:

- Define the RVE Geometry and Material Properties:
  - Identify the RVE dimensions, including the distribution of voids (e.g., spheres) and reinforcement.
  - Assign material properties such as Young's modulus E, Poisson's ratio v, and shear modulus G to each material in the RVE.
- Finite Element Mesh:

- o Generate a 3D finite element mesh of the RVE, ensuring adequate resolution for accurate results.
  - o Use e.g. 8-node hexahedral elements for the mesh to capture the geometry and material distributions effectively.
- Compute the Condensed Stiffness Matrix ($\mathbf{K}_e$):
  - o Assemble the global stiffness matrix $\mathbf{K}$ by integrating the element stiffness matrices $\mathbf{k}_e$ over the RVE domain.
  - o Include material heterogeneities and voids as defined by the material map.
- Transformation to Effective Parameters:
  - o Use a displacement-strain transformation matrix $\mathbf{H}$ to relate local displacements to macroscopic strains. Transformation matrix $\mathbf{H}$ combines general strains $\boldsymbol{\epsilon} = \left[\varepsilon_x, \varepsilon_y, \gamma_{xy}\gamma_{xz}, \gamma_{yz}, \kappa_x, \kappa_y, \kappa_{xy}\right]^T$ and displacement $d = [u, v, w]^T$. For a node i located at (x, y, z), and is defined as:

$$\mathbf{H}_i = \begin{bmatrix} x & 0 & y/2 & z/2 & 0 & xz & 0 & yz/2 \\ 0 & y & x/2 & 0 & z/2 & 0 & yz & xz/2 \\ 0 & 0 & 0 & x/2 & y/2 & -x^2/2 & -y^2/2 & -xy/2 \end{bmatrix} \tag{2.1}$$

  - o Compute the effective stiffness matrix **ABDR** using:

$$\mathbf{ABDR} = \frac{\mathbf{H}^T \cdot \mathbf{K}_e \cdot \mathbf{H}}{area} \tag{2.2}$$

    where $area$ is the surface area of the RVE in the xy-plane.
- Extract Effective Parameters:
  - o Divide the effective stiffness matrix into submatrices representing in-plane stiffness (**A**), coupling term (**B**), bending stiffness (**D**), and transverse shear stiffness (**R**).

This homogenization approach provides a computationally efficient way to represent complex 3D structures like Bubble Deck slabs using simplified 2D models while maintaining accuracy in displacement and stiffness predictions.

Below, a concise outline of the process for calculating the condensed stiffness matrix is presented. This method focuses on transforming the detailed 3D stiffness representation of a structure, such as an RVE, into a reduced form suitable for numerical homogenization. The procedure leverages the finite element method to efficiently capture the essential mechanical behaviour of the model while reducing computational complexity. By condensing the stiffness matrix, the approach simplifies the representation of the internal and external degrees of freedom, enabling effective parameter extraction that accurately reflects the structural response of the full model. This process forms the foundation for developing equivalent 2D representations of complex 3D structures.

The mains steps are:
- Define Element Geometry:
  - o For an 8-node hexahedral element, the geometry is interpolated using shape functions N_i, which are functions of natural coordinates ξ, η, ζ in the range $\xi \in [-1,1]$, $\eta \in [-1,1]$, $\zeta \in [-1,1]$:

$$N_i(\xi, \eta, \zeta) = \frac{1}{8}(1 + \xi_i\xi)(1 + \eta_i\eta)(1 + \zeta_i\zeta) \tag{2.3}$$

    where ξ_i, η_i, ζ_i are the natural coordinates of node i.

- Compute Strain-Displacement Matrix ($\mathbf{B}_s$):
  - The strain-displacement matrix relates nodal displacements to strains in the element:

$$\mathbf{B}_s = \begin{bmatrix} \dfrac{\partial N_1}{\partial x} & 0 & 0 & \dots & \dfrac{\partial N_8}{\partial x} & 0 & 0 \\[2mm] 0 & \dfrac{\partial N_1}{\partial y} & 0 & \dots & 0 & \dfrac{\partial N_8}{\partial y} & 0 \\[2mm] 0 & 0 & \dfrac{\partial N_1}{\partial z} & \dots & 0 & 0 & \dfrac{\partial N_8}{\partial z} \\[2mm] \dfrac{\partial N_1}{\partial y} & \dfrac{\partial N_1}{\partial x} & 0 & \dots & \dfrac{\partial N_8}{\partial y} & \dfrac{\partial N_8}{\partial x} & 0 \\[2mm] 0 & \dfrac{\partial N_1}{\partial z} & \dfrac{\partial N_1}{\partial y} & \dots & 0 & \dfrac{\partial N_8}{\partial z} & \dfrac{\partial N_8}{\partial y} \\[2mm] \dfrac{\partial N_1}{\partial z} & 0 & \dfrac{\partial N_1}{\partial x} & \dots & \dfrac{\partial N_8}{\partial z} & 0 & \dfrac{\partial N_8}{\partial x} \end{bmatrix} \tag{2.4}$$

  - The derivatives $\frac{\partial N_i}{\partial x}, \frac{\partial N_i}{\partial y}, \frac{\partial N_i}{\partial z}$ are computed using the Jacobian transformation:

$$\frac{\partial \mathbf{N}}{\partial x} = \mathbf{J}^{-1} \frac{\partial N}{\partial \xi}, \quad \mathbf{J} = \frac{\partial x}{\partial \xi} \tag{2.5}$$

- Define Material Stiffness Matrix ($\mathbf{D}_m$):
  - For isotropic materials:

$$\mathbf{D}_m = \frac{E}{(1+\nu)(1-2\nu)} \begin{bmatrix} 1-\nu & \nu & \nu & 0 & 0 & 0 \\ \nu & 1-\nu & \nu & 0 & 0 & 0 \\ \nu & \nu & 1-\nu & 0 & 0 & 0 \\ 0 & 0 & 0 & \dfrac{1-2\nu}{2} & 0 & 0 \\ 0 & 0 & 0 & 0 & \dfrac{1-2\nu}{2} & 0 \\ 0 & 0 & 0 & 0 & 0 & \dfrac{1-2\nu}{2} \end{bmatrix} \tag{2.6}$$

  - E: Young's modulus, ν: Poisson's ratio.
- Formulate Element Stiffness Matrix ($\mathbf{k}_e$):
  - Using numerical integration (e.g., Gauss quadrature) over the volume of the element:

$$\mathbf{k}_e = \int_V \mathbf{B}_s^T \mathbf{D}_m \mathbf{B}_s \, dV \tag{2.7}$$

  - Approximated as:

$$\mathbf{k}_e = \sum_{i=1}^{n} w_i \, \mathbf{B}_s^T \mathbf{D}_m \mathbf{B}_s \, |\mathbf{J}| \tag{2.8}$$

   where w_i are the Gauss weights, and $|\mathbf{J}|$ is the determinant of the Jacobian.
- Assemble Global Stiffness Matrix ($\mathbf{K}$):

- Combine $\mathbf{k}_e$ for all elements into a global matrix $\mathbf{K}$ based on connectivity and degrees of freedom.
- Apply Static Condensation:
  - Define External Nodes: The external nodes are defined as those located on the side surfaces of the RVE.
  - Define Degrees Of Freedom (DOF) for external and internal nodes.
  - Static Condensation Equation: The condensed stiffness matrix $\mathbf{K}_e$ is calculated as:

$$\mathbf{K}_e = \mathbf{K}_{ee} - \mathbf{K}_{ei} \cdot \mathbf{K}_{ii}^{-1} \cdot \mathbf{K}_{ie} \tag{2.9}$$

where:
$\mathbf{K}_{ee} = \mathbf{K}(e, e)$: Submatrix for external DOFs,
$\mathbf{K}_{ii} = \mathbf{K}(i, i)$: Submatrix for internal DOFs,
$\mathbf{K}_{ei} = \mathbf{K}(e, i)$ and $\mathbf{K}_{ie} = \mathbf{K}(i, e)$: Coupling submatrices.

2.4. Homogenization through spatial integration

Homogenization through spatial integration is a method used to derive effective material properties by averaging the mechanical behaviour of a heterogeneous structure over its volume. Instead of relying on detailed numerical models for every microscopic feature, this approach computes macroscopic properties by integrating stresses, strains, or stiffness matrices across the spatial domain of the Representative Volume Element (RVE). This enables the determination of equivalent material parameters, such as effective stiffness or compliance, that capture the overall response of complex materials, making it particularly useful for modelling composites or perforated structures like Bubble Deck slabs.

The integral form of the centre of gravity calculation, incorporating material properties and spatial coordinates x, y, and z, results from the weighted summation of the z-coordinate for the centre of gravity divided by the summation of material stiffness contributions:

$$z_0 = \frac{\iiint_\Omega E(x, y, z) \cdot z_c \, dx \, dy \, dz}{\iiint_\Omega E(x, y, z) dx \, dy \, dz}, \tag{2.10}$$

where:
- $E(x, y, z)$ is the Young's modulus at position (x, y, z), as determined by the material map for concrete, steel and for voids.
- z_c is the z-coordinate of the centroid of the element at (x, y, z).
- Ω is the domain of the RVE.

As was already mentioned previously The effective matrix **ABD** matrix can be expanded to include the transverse shear stiffness matrix **R**, making it an **ABDR**. The explanation of its components is as follows:
- Matrix **A** (Membrane Stiffness) - relates in-plane forces (N_x, N_y, N_{xy}) to mid-plane strains $(\epsilon_x, \epsilon_y, \gamma_{xy})$.
- Matrix **B** (Coupling Stiffness) - relates in-plane forces (N_x, N_y, N_{xy}) to bending curvatures $(\kappa_x, \kappa_y, \kappa_{xy})$, and bending moments (M_x, M_y, M_{xy}) to mid-plane strains $(\varepsilon_x, \varepsilon_y, \gamma_{xy})$.
- Matrix **D** (Bending Stiffness) - relates bending moments (M_x, M_y, M_{xy}) to curvatures $(\kappa_x, \kappa_y, \kappa_{xy})$.
- Matrix **R** (Transverse Shear Stiffness) - relates transverse shear forces (Q_x, Q_y) to transverse shear strains $(\gamma_{xz}, \gamma_{yz})$.

- Structure of the **ABDR** Matrix:

$$\mathbf{ABDR} = \begin{bmatrix} \mathbf{A} & \mathbf{B} & 0 \\ \mathbf{B} & \mathbf{D} & 0 \\ 0 & 0 & \mathbf{R} \end{bmatrix} \tag{2.11}$$

In order to compute the stiffness matrix components for a RVE the integral formulations are used. These formulations enable the translation of a complex 3D structure into equivalent 2D parameters that accurately reflect its mechanical behaviour. By integrating material properties and accounting for geometric and positional factors, effective in-plane stiffness, bending stiffness, and transverse shear stiffness are determined. For homogeneous RVEs without voids or reinforcements, these equations simplify, providing direct relationships between stiffness components and the plate's thickness. The main steps has to be followed:

- Material stiffness in-plane

$$\mathbf{Q}(x, y, z) = \frac{E_i}{1 - v_i^2} \cdot \begin{bmatrix} 1 & v_i & 0 \\ v_i & 1 & 0 \\ 0 & 0 & \frac{1 - v_i}{2} \end{bmatrix} \tag{2.12}$$

- Transversal stiffness:

$$\mathbf{G}(x, y, z) = \frac{5}{6} \begin{bmatrix} G_i & 0 \\ 0 & G_i \end{bmatrix} \tag{2.13}$$

- Membrane stiffness (**A**):

$$\mathbf{A} = \frac{1}{area} \iiint_{\Omega} \mathbf{Q}(x, y, z) \, dx \, dy \, dz \tag{2.14}$$

- Bending stiffness (**D**) (i.e. weighted moment of inertia about z_0):

$$\mathbf{D} = \frac{1}{area} \iiint_{\Omega} \mathbf{Q}(x, y, z) \cdot (z_i - z_0)^2 dx \, dy \, dz \tag{2.15}$$

- Transverse shear stiffness (**R**):

$$\mathbf{R} = \frac{1}{area} \iiint_{\Omega} \mathbf{G}(x, y, z) dx \, dy \, dz \tag{2.16}$$

where:
- z_i: z-coordinate of the centre of each element.
- $E_i = E(x, y, z)$: Young's modulus for material at location (x, y, z).
- $G_i = G(x, y, z)$: Kirchhoff's modulus for material at location (x, y, z).
- $v_i = v(x, y, z)$: Poisson's ratio for material at location (x, y, z).
- z_0: Initial z-centre of gravity (relative to the $xy-$plane).
- $area$: surface area of the RVE base (in $xy-$plane).

For the homogeneous RVE (no voids nor rebars) the above equations can be simplified, so the matrices **A**, **B**, **D** and **R** are:

$$\mathbf{A} = \mathbf{Q} \cdot h, \quad \mathbf{B} = 0, \quad \mathbf{D} = \mathbf{Q} \cdot \frac{h^3}{12}, \quad \mathbf{R} = \mathbf{G} \cdot h \tag{2.17}$$

2.5. Full 3D numerical model of Bubble Deck slab

A comprehensive 3D finite element model was developed in Abaqus 2023 to precisely replicate the experimental slab. The model fully reflects the real-world configuration, including 17 × 34 spherical voids (see Figure 3a) representing ping-pong balls and reinforcement in the form of a mesh of Ø3 mm bars, spaced at 30 mm intervals (see Figure 3c), both at the top and bottom of the slab, with a 15 mm offset from the surfaces. The voids and reinforcement are positioned exactly as in the physical slab, ensuring an accurate representation of the structure (see Figure 3b).

After meshing the reinforcement, additional beam elements were included in the model, resulting in the following mesh statistics:

- Total number of nodes: 1,268,986
- Total number of elements: 855,298, comprising:
  - 18496 linear line elements of type B31 (for reinforcement bars)
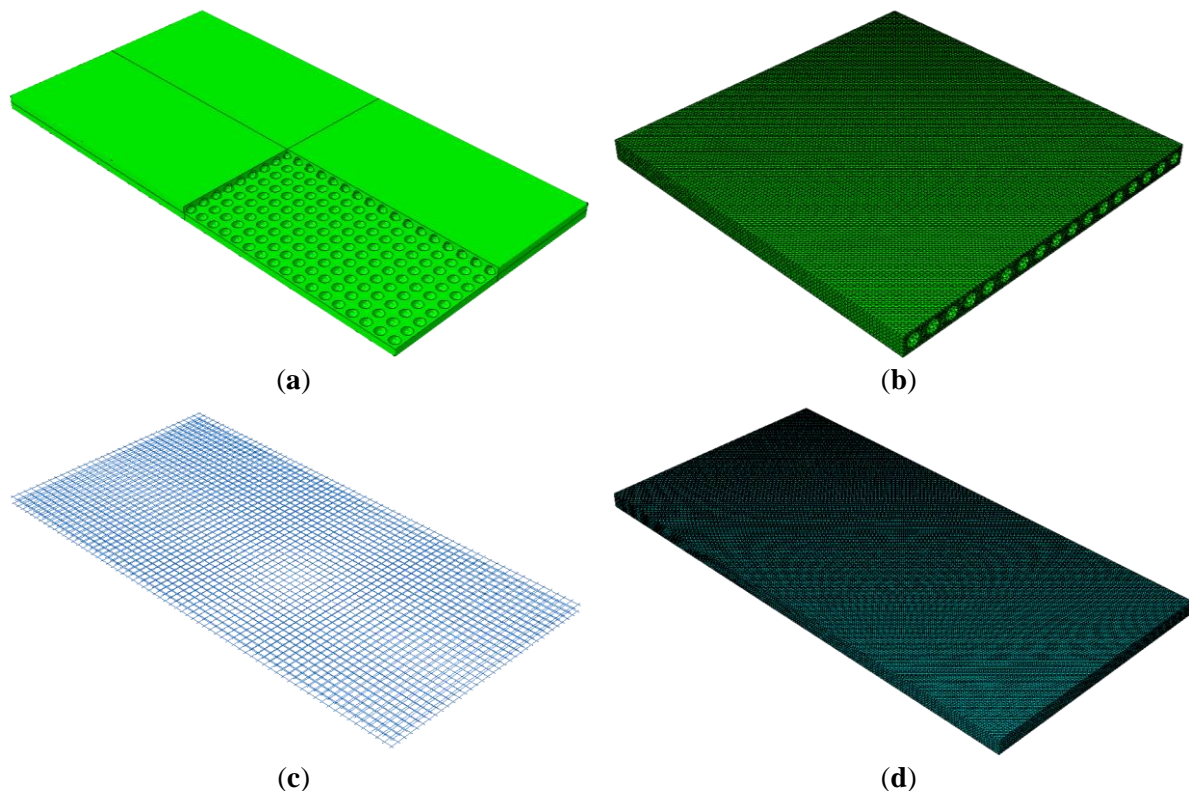 - 836,802 quadratic tetrahedral elements of type C3D10 (for the slab and voids, see Figure 3d)

(**a**) (**b**)

(**c**) (**d**)

Fig. 3. Visualization of different slab configurations and their mesh representations. (**a**) schematic representation of the slab with spherical voids and reinforcement bars. (**b**) Meshed model of the slab showing the distribution of voids and reinforcement in detail. (**c**) view of the net of top and bottom reinforcement bars. (**d**) Full 3D mesh model capturing all geometric and material details

The embedded beam elements for the reinforcement introduces additional degrees of freedom. Each node of the tetrahedral elements has three degrees of freedom, while nodes of the beam elements have six degrees of freedom. This high-resolution model accurately captures the mechanical behaviour

of the slab and its reinforcement under various loading conditions. While computationally demanding, it provides critical insights into stress distribution, deformation, and interaction effects between the slab and reinforcement, serving as a benchmark for validating experimental and simplified numerical models.

2.6.   Simplified numerical model of Bubble Deck slab

The simplified finite element model represents a computationally efficient alternative to the full 3D model, designed to reduce the computational burden while maintaining an adequate level of accuracy for specific analyses. The model consists of:

- Total number of elements: 2312 four-node shell elements,
- Total number of nodes: 2415, each with six degrees of freedom (DOF), see Figure 4.

The total number of degrees of freedom for the simplified model is: 6×2415=14,490 DOF's, which is approximately 265 times less compared to full 3D model consisting of approximately 4 million DOF's. This represents a reduction by more than two orders of magnitude, significantly decreasing computational time and resource requirements.
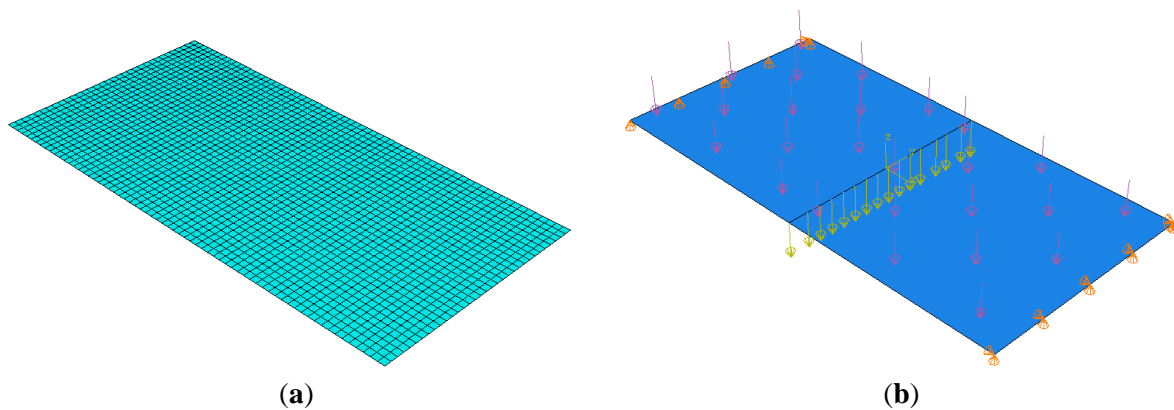

(**a**)   (**b**)

Fig. 4. Simplified model: (a) mesh representation of the slab model; (b) loads and boundary conditions

The simplified model employs four-point Gauss quadrature with selective integration to eliminate the shear locking effect, which can distort results in thin shell elements under bending-dominated conditions. This approach ensures accurate stiffness representation while maintaining computational efficiency.

The model directly utilizes the **ABDR** stiffness matrix (already explained in details in previous sections), which encapsulates in-plane stiffness (**A**), bending stiffness (**D**), and transverse shear stiffness (**R**), without the need to define an equivalent thickness or effective constitutive parameters. By avoiding these approximations, the model maintains fidelity to the mechanics of the problem within its scope. However, s significant limitation of this approach is its inability to directly compute stresses within the structure. Instead, the simplified model can determine accurately nodal displacements and rotations, general strains as well as determine:

- Normal forces $\left(N_x, N_y, N_{xy}\right)$
- Shear forces $\left(Q_x, Q_y\right)$
- Bending moments $\left(M_x, M_y, M_{xy}\right)$.

The relationship for these quantities is given by:

$$\begin{bmatrix} N_x \\ N_y \\ N_{xy} \\ M_x \\ M_y \\ M_{xy} \\ Q_x \\ Q_y \end{bmatrix} = \begin{bmatrix} \begin{bmatrix} A_{11} & A_{12} & 0 \\ A_{21} & A_{22} & 0 \\ 0 & 0 & A_{33} \end{bmatrix} & \mathbf{B} = \mathbf{0}_{3\times3} & \mathbf{0}_{3\times2} \\ \mathbf{B} = \mathbf{0}_{3\times3} & \begin{bmatrix} D_{11} & D_{12} & 0 \\ D_{21} & D_{22} & 0 \\ 0 & 0 & D_{33} \end{bmatrix} & \mathbf{0}_{3\times2} \\ \mathbf{0}_{2\times3} & \mathbf{0}_{2\times3} & \begin{bmatrix} R_{11} & 0 \\ 0 & R_{22} \end{bmatrix} \end{bmatrix} \begin{bmatrix} \varepsilon_x \\ \varepsilon_y \\ \gamma_{xy} \\ \kappa_x \\ \kappa_y \\ \kappa_{xy} \\ \gamma_{xz} \\ \gamma_{yz} \end{bmatrix} \tag{2.18}$$

Here:
- $\mathbf{A}, \mathbf{B}, \mathbf{D}, \mathbf{R}$ are the extensional, coupling, bending, and transverse shear stiffness matrices, respectively.
- ϵ, κ, γ represent membrane strains, curvatures, and transverse shear strains, which are computed in each Gauss point of each element based on nodal displacements.

The displacements (u, v, w) and rotations (θ_x, θ_y) at the nodes are obtained by solving the finite element equilibrium equations:

$$\mathbf{K} \cdot \mathbf{u} = \mathbf{F} \quad \rightarrow \quad \mathbf{u} = \mathbf{K}^{-1}\mathbf{F} \tag{2.19}$$

where:
- $\mathbf{K}$: Global stiffness matrix (explained already in previous section),
- $\mathbf{u}$: Global nodal displacement vector (including translations and rotations),
- $\mathbf{F}$: Global force vector.

Once $\mathbf{u}$ is computed, the displacements and rotations at each node are extracted directly from the vector. Strains at a specific point within an element (here at 4 Gauss points in each element) are calculated using the strain-displacement matrix ($\mathbf{B}_s$) and the nodal displacement vector ($\mathbf{u}_e$):

$$\epsilon = \mathbf{B}_s \cdot \mathbf{u}_e \tag{2.20}$$

where:
- $\epsilon = \left[\varepsilon_x, \varepsilon_y, \gamma_{xy}, \kappa_x, \kappa_y, \kappa_{xy}, \gamma_{xz}, \gamma_{yz}\right]^T$: Strain vector (membrane, bending, and shear components),
- $\mathbf{B}_s$: Strain-displacement matrix,
- $\mathbf{u}_e$: Element nodal displacement vector.

In case of 4-node shell elements (differently as in case of 8-node hexahedral element) the strain-displacement matrix is divided into components for membrane ($\mathbf{B}_m$), bending ($\mathbf{B}_b$), and shear ($\mathbf{B}_r$) strains:

Membrane Strains (ϵ_m):

$$\mathbf{B}_m = \begin{bmatrix} \dfrac{\partial N_1}{\partial x} & 0 & 0 & 0 & 0 & \dots & \dfrac{\partial N_4}{\partial x} & 0 & 0 & 0 & 0 \\ 0 & \dfrac{\partial N_1}{\partial y} & 0 & 0 & 0 & \dots & 0 & \dfrac{\partial N_4}{\partial y} & 0 & 0 & 0 \\ \dfrac{\partial N_1}{\partial y} & \dfrac{\partial N_1}{\partial x} & 0 & 0 & 0 & \dots & \dfrac{\partial N_4}{\partial y} & \dfrac{\partial N_4}{\partial x} & 0 & 0 & 0 \end{bmatrix} \tag{2.21}$$

Bending Strains (κ):

$$\mathbf{B}_b = \begin{bmatrix} 0 & 0 & 0 & \dfrac{\partial N_1}{\partial x} & 0 & \ldots & 0 & 0 & 0 & \dfrac{\partial N_4}{\partial x} & 0 \\ 0 & 0 & 0 & 0 & \dfrac{\partial N_1}{\partial y} & \ldots & 0 & 0 & 0 & 0 & \dfrac{\partial N_4}{\partial y} \\ 0 & 0 & 0 & \dfrac{\partial N_1}{\partial y} & \dfrac{\partial N_1}{\partial x} & \ldots & 0 & 0 & 0 & \dfrac{\partial N_4}{\partial y} & \dfrac{\partial N_4}{\partial x} \end{bmatrix} \tag{2.22}$$

Shear Strains ($\boldsymbol{\gamma}$):

$$\mathbf{B}_r = \begin{bmatrix} 0 & 0 & \dfrac{\partial N_1}{\partial x} & 0 & -N_1 & 0 & \ldots & 0 & 0 & \dfrac{\partial N_4}{\partial x} & -N_4 & 0 \\ 0 & 0 & \dfrac{\partial N_1}{\partial y} & 0 & -N_1 & \ldots & 0 & 0 & \dfrac{\partial N_4}{\partial y} & 0 & -N_4 \end{bmatrix} \tag{2.23}$$

These matrices are combined into a global $\mathbf{B}_s$ matrix:

$$\boldsymbol{B}_s = \begin{bmatrix} \boldsymbol{B}_m \\ \boldsymbol{B}_b \\ \boldsymbol{B}_r \end{bmatrix} \tag{2.24}$$

The shape functions $\mathbf{N}$ and their derivatives $\partial \mathbf{N}/\partial \mathbf{x}$ are computed in the same manner as described in the previous equations for 8-node hexahedral or 4-node shell elements, using natural coordinates and the Jacobian transformation, see Equation (2.5). This ensures consistency in the formulation of the strain-displacement relationship across different elements. By leveraging these shape functions and derivatives, the $\mathbf{B}_s$ matrix accurately represents the strain distribution within each element.

In the simplified model, shear locking can occur due to the over-constrained nature of the transverse shear stiffness when using standard finite element formulations. To mitigate this issue, selective reduced integration is applied to the shear-related terms in the $\mathbf{B}_r$ matrix of the shell elements, ensuring accurate shear deformation representation without introducing spurious stiffness. This approach improves the overall accuracy and convergence of the simplified model.

3. RESULTS AND DISCUSSION

3.1.   Validation of Homogenization Methods with Analytical Models

To validate the accuracy and reliability of the proposed homogenization methods, a simplified benchmark example is analysed. The model consists of a fully concrete slab with a thickness of 60 mm, where the Representative Volume Element (RVE) is a cube with dimensions of 60×60×60 mm. This setup removes the complexity introduced by voids and reinforcement, enabling direct comparison of results with analytical solutions for a homogeneous material. The concrete properties used in the model are consistent with the material parameters defined earlier in the study.

The comparison includes numerical homogenization, which relies on finite element discretization of the RVE, and homogenization through spatial integration, which analytically calculates effective stiffness parameters by integrating over the RVE domain. Both approaches are evaluated against theoretical predictions for a homogeneous concrete slab to assess their precision. This benchmark case provides a critical foundation for understanding the performance of the homogenization methods in more complex configurations. By validating these methods with an analytically tractable case, their applicability to

more realistic scenarios, such as voided slabs with reinforcement, can be established with greater confidence.

The calculated stiffness values for the C20/25 concrete RVE are as follows:

- Axial stiffness (EA): $E/(1 - v^2) \cdot t = 1.562 \cdot 10^6$ N/mm
- Bending stiffness (EI): $E/(1 - v^2) \cdot t^3/12 = 4.687 \cdot 10^8$ Nmm
- Transverse shear stiffness (GA): $5/6 \cdot E/2(1 + v) \cdot t = 0.521 \cdot 10^6$ N/mm

These values are based on a concrete slab with a thickness (t) of 60 mm and a Young's modulus of 25 GPa.

Table 2. Validation of homogenization using spatial integration. The table shows the computed stiffness values (EA, EI, GA), corresponding errors compared to theoretical values, and the number of nodes in the model

number	EA [N]	EI [Nmm²]	GA [N]	Error [%]		
of nodes	×10⁻⁶	×10⁻⁶	×10⁻⁶	EA	EI	GA
216	1.148	577.8	0.383	-26.53	23.27	-25.41
1,728	1.331	485.9	0.444	-14.79	3.66	-13.49
27,000	1.463	470.3	0.488	-6.35	0.32	-4.91
216,000	1.512	469.0	0.504	-3.25	0.06	-1.77
1,728,000	1.537	468.8	0.512	-1.64	0.01	-0.14
13,824,000	1.550	468.8	0.517	-0.83	0.00	0.69

The results obtained using spatial integration for homogenization (see Table 2 and Fig. 5) demonstrate a clear trend of convergence as the number of nodes increases. For the smallest model with 216 nodes, significant errors are observed in all stiffness components (EA:−26.53%, EI:23.27%, GA:−25.41%) due to the coarse discretization of the geometry. However, as the node count increases to 1,728 and beyond, the accuracy improves significantly, with errors for the largest model (13,824,000 nodes) dropping to less than 1% for EA and EI, and slightly higher for GA (0.69%). This demonstrates the effectiveness of the integration approach in capturing the effective stiffness parameters with high fidelity, provided sufficient spatial resolution is employed. Notably, the error for GA converges more slowly, reflecting the inherent sensitivity of shear stiffness to discretization.

The results from numerical homogenization (see Table 3 and Fig. 6) show a similar trend, with errors decreasing as the number of degrees of freedom (DOFs) increases. However, the initial errors for coarse models (e.g., 192 DOFs) are relatively low compared to the spatial integration approach, particularly for EA (3.94%3) and EI (7.74%). This indicates that finite element models can capture stiffness parameters reasonably well even with a coarser mesh. As the DOFs increase to 89,373, the errors reduce further, with EA and EI stabilizing around 3% and 1.5%, respectively. However, the error for GA remains higher (−10.08%) and converges more slowly, consistent with the challenges in modelling transverse shear stiffness in numerical methods.

Table 3. Validation of numerical homogenization using finite elements. The table presents the computed stiffness values (EA, EI, GA), their respective errors, and the number of degrees of freedom (DOFs) in each model

number of DOF's	EA [N] ·10⁻⁶	EI [Nmm²] ·10⁻⁶	GA [N] ·10⁻⁶	Error [%]		
				EA	EI	GA
192	1.624	505.0	0.513	3.94	7.74	-1.51
1,029	1.615	484.1	0.478	3.36	3.28	-8.05
6,591	1.611	478.1	0.466	3.12	1.99	-9.13
12,288	1.611	477.2	0.464	3.07	1.81	-9.51
27,783	1.610	476.6	0.463	3.03	1.66	-9.82
89,373	1.609	476.0	0.461	3.00	1.55	-10.08

Both methods show improved accuracy with increased resolution. Spatial integration achieves superior accuracy for large models, particularly for EA and EI, as it does not rely on solving large matrix systems. In contrast, numerical homogenization provides acceptable accuracy even for smaller models, making it computationally advantageous for preliminary analyses. However, both methods struggle with GA, with numerical homogenization showing consistently higher errors. This suggests that additional refinement or alternative approaches may be required for accurately modelling transverse shear stiffness.
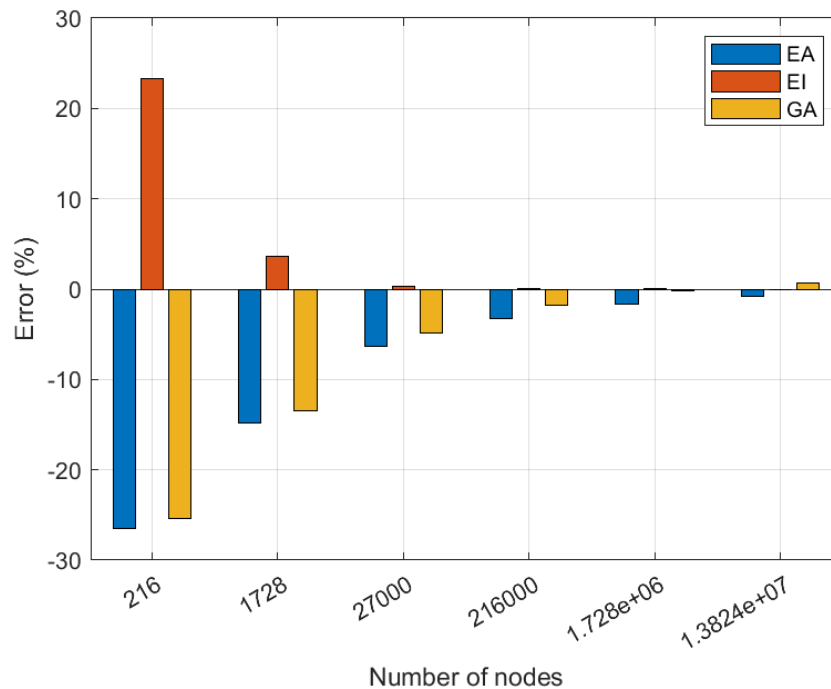

Fig. 5. Error trends in stiffness parameters (EA, EI, GA) for spatial integration homogenization as a function of the number of nodes. The figure illustrates the convergence of the errors as the model resolution increases

The observed inaccuracies in the calibration of transverse shear stiffness arise from the inherent assumptions of the homogenization method based on energy principles. Specifically, the tangential interactions are condensed to nodes located on the lateral surfaces of the Representative Volume Element (RVE). This approach, while computationally efficient, does not fully capture the distribution of shear stresses, leading to approximation errors. A potential solution to reduce these inaccuracies involves selecting nodes on the upper and lower surfaces of the RVE. However, such a modification compromises the method's universality and flexibility across different applications. To address this, an appropriately refined finite element mesh is recommended, as it enables a more precise representation of the material's mechanical behaviour while maintaining the robustness of the homogenization framework.
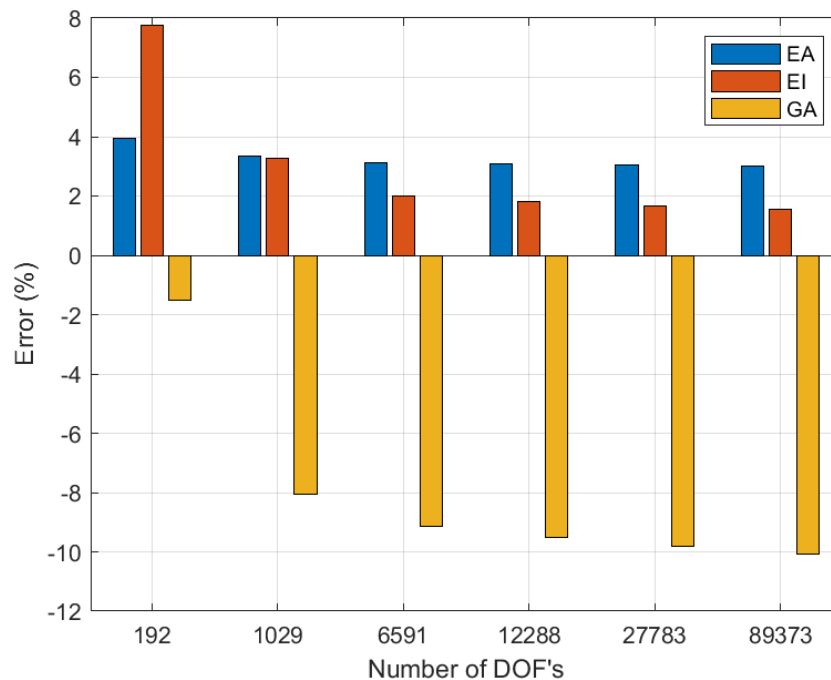

Fig. 6. Error trends in stiffness parameters (EA, EI, GA) for numerical homogenization as a function of the number of DOFs. The figure highlights the decreasing errors with increasing model complexity

3.2. Comparison of Full 3D and Simplified Model for Deflection Analysis

The numerical analyses using the full 3D model and the simplified model based on the ABDR matrix highlight the differences in their ability to predict structural behaviour. The simplified model employs homogenized stiffness values derived using spatial integration from 778,688 points, including the effects of reinforcement bars and spherical voids. The **ABDR** components are as follows:

- A matrix:

$$\mathbf{A} = \begin{bmatrix} 1.4887 & 0.3189 & 0 \\ 0.3189 & 0 & 0 \\ 0 & 0 & 0.5849 \end{bmatrix} \times 10^6 \, \text{N/mm} \tag{3.1}$$

- D matrix:

$$\mathbf{D} = \begin{bmatrix} 479.32 & 99.10 & 0 \\ 99.10 & 479.32 & 0 \\ 0 & 0 & 190.11 \end{bmatrix} \times 10^8 \text{ Nmm} \tag{3.2}$$

- R matrix:

$$\mathbf{R} = \begin{bmatrix} 0.487 & 0 \\ 0 & 0.487 \end{bmatrix} \times 10^6 \text{ N/mm} \tag{3.3}$$

The homogenized value ($A_{11} = 1.4887 \times 10^6$ N/mm) is approximately 4.7% lower than the theoretical reference value. This reduction reflects the influence of voids and reinforcement, which decrease the effective stiffness. The homogenized value ($D_{11} = 479.32 \times 10^8$ Nmm) is slightly higher than the theoretical value by 2.3%. This increase may result from the reinforcement bars compensating for the stiffness loss due to voids. The homogenized value ($R_{11} = 4.874 \times 10^5$ N/mm) is 6.4% lower than the theoretical reference. This reduction highlights the sensitivity of shear stiffness to heterogeneities in the structure.
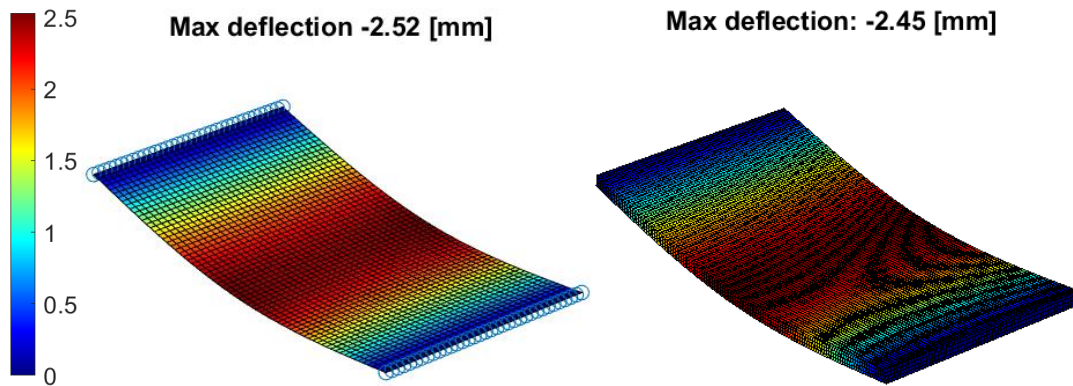

Fig. 7. Comparison of deflection maps for the full 3D model and the simplified ABDR model. The maximum deflections predicted are −2.45 mm (full 3D model) and −2.52 mm (simplified model), closely aligning with the experimentally measured deflection of −2.59 mm

The full 3D model predicts a maximum deflection of −2.45 mm. This result captures the detailed interaction between voids, reinforcement, and concrete material, making it more accurate but computationally demanding. The simplified model predicts a maximum deflection of −2.52 mm, slightly higher than the full 3D model (Fig. 7). The discrepancy (∼2.8%) is within acceptable limits, demonstrating that the simplified model is effective for global deflection predictions, despite its inability to provide detailed stress or strain distributions. Both models exhibit similar deflection patterns, with the highest values concentrated at the centre of the slab, indicating good agreement in global behaviour. For a slab with dimensions 1020×2040 mm, freely supported along shorter edges and subjected to self-weight and a line load of 500 kg at mid-span:

$$q_{self} = 1.2414 \times 10^{-3} \frac{\text{N}}{\text{mm}^2} \tag{3.4}$$

Line load converted to N/m:

$$q_{line} = 4.905 \text{ N/mm} \tag{3.5}$$

Maximum deflection (δ_{max}) using the theoretical bending stiffness:

$$\delta_{max} = \frac{q_{line}\, L^3}{48\, D_{11}} + \frac{5\, q_{self}\, L^4}{384\, D_{11}} = 0.879 + 1.845 = 2.724 \text{ mm} \tag{3.6}$$

The calculated maximum deflection of the slab under self-weight and a line load of 500 kg at mid-span is approximately 2.72 mm. This value aligns closely with the numerical results from both the full 3D model (2.45 mm) and the simplified ABDR model (2.52 mm), indicating that both numerical approaches effectively capture the global behaviour of the slab.

Table 4. Comparison of Deflection Results from Experimental, Numerical, and Analytical Approaches

Approach	Deflection [mm]	Error [%]
Experimental measurement	2.59	--
Full 3D model	2.45	-5.41
Simplified ABDR model	2.52	-2.70
Analytical calculation	2.72	5.02

The experimental measurement of the slab's deflection under self-weight and an additional line load of 500 kg yielded a maximum deflection of **2.59 mm**. This value lies between the predictions of the full 3D model (2.45 mm) and the simplified ABDR model (2.52 mm). The analytical calculation, based on the theoretical bending stiffness of the slab, provided a slightly higher deflection of 2.72mm (Table 4).

4. CONCLUSIONS

The comparison highlights the effectiveness of both numerical approaches in predicting the global deflection of the slab. The full 3D model, while computationally intensive, provides highly detailed insights into the interaction between voids, reinforcement, and concrete. Its slight underprediction of the deflection may be attributed to the assumptions and boundary conditions in the numerical setup, as well as the idealized material properties. On the other hand, the simplified ABDR model demonstrates a high degree of accuracy in capturing the slab's deflection while being computationally efficient. Its homogenized stiffness parameters, derived from spatial integration, effectively represent the global response of the structure.

The experimental deflection (2.59 mm) validates the reliability of the numerical models, with both the full 3D and ABDR approaches showing errors below or close to 5% relative to the measured value. This confirms that the simplified ABDR model, despite its inability to provide local stress and strain distributions, is a valuable tool for preliminary design and analysis of complex structures such as slabs with voids and reinforcement. Moving forward, integrating experimental validation with numerical modelling will enhance the robustness of predictions, particularly in scenarios where the computational cost of a full 3D model is prohibitive.

REFERENCES

1. Korkmaz, HH and Tankut, T 2005. Performance of a precast concrete beam-to-beam connection subject to reversed cyclic loading. *Engineering Structures* **27**, 1392–1407.
2. Feng, D, Wu, G and Lu, Y 2018. Finite element modelling approach for precast reinforced concrete beam-to-column connections under cyclic loading. *Engineering Structures* **174**, 49–66.
3. Newell, S and Goggins, J 2019. Experimental study of hybrid precast concrete lattice girder floor at construction stage. *Structures* **20**, 866–885.
4. Lichołai, L et al. 2008. Budownictwo Ogólne. Tom 3. Elementy Budynków. Podstawy Projektowania [General Construction, volume 3, Elements of Buildings. Fundamentals of Design], Warsaw, Arkady, Poland (In Polish).
5. Derkowski, W and Skalski, P 2017. New concept of slimfloor with prestressed composite beams. *Procedia Engineering* **193**, 176–183.
6. Baran, E 2015. Effects of cast-in-place concrete topping on flexural response of precast concrete hollow-core slabs. *Engineering Structure* **98**, 109–117.
7. Quraisyah, ADS, Kartini, K, Hamidah, MS and Daiana, K 2020. Bubble Deck Slab as an Innovative Biaxial Hollow Slab—A Review. *Journal of Physics: Conference Series* **1711**, 012003.
8. Shetkar, A and Hanche, N 2015. An Experimental Study on Bubble Deck Slab System with Elliptical Balls. *Indian Journal of Scientific Research* **12**, 21–27.
9. Tiwari, N and Zafar, S 2016. Structural Behaviour of Bubble Deck Slabs and Its Application: An Overview. *International Journal of Science and Research Development* **4**, 433–437.
10. Mahalakshmi, S and Nanthini, S 2017. Bubble Deck. International Journal for Research in Applied Science & Engineering Technology **5**, 580–588.
11. Abishek, V and Iyappan, GR 2021. Study on flexural behavior of bubble deck slab strengthened with FRP. *Journal of Physics: Conference Series* **2040**, 012018.
12. Mirajkar, S, Balapure, M and Kshirsagar, T 2017. Study of Bubble Deck Slab. *International Journal of Research in Science & Engineering* **7**, 1–5.
13. Konuri, S and Varalakshmi, TVS 2019. Review on Bubble Deck Slabs Technology and their Applications. *International Journal of Scientific & Technology Research* **8**, 427–432.
14. Ksit, B and Szymczak-Graczyk, A 2019. Rare weather phenomena and the work of large-format roof coverings. *Civil Environmental Engineering Reports* **29**, 123–133.
15. Szymczak-Graczyk, A, Ksit, B and Laks, I 2019. Operational Problems in Structural Nodes of Reinforced Concrete Constructions. *IOP Conference Series: Materials Science and Engineering* **603**, 032096.
16. Markiewicz, P 2009. Budownictwo Ogólne dla Architektów [General Building Construction for Architects], Cracow, Archi-Plus, Poland (In Polish).
17. Szydłowski, R 2018. Concrete properties for long-span post-tensioned slabs. International Symposium on Advanced Material Research, Jeju Island, Republic of Korea.
18. Bhowmik, R, Mukherjee, S and Das, A 2017. Banerjee, S. Review on Bubble Deck with Spherical Hollow Balls. *International Journal of Civil Engineering and Technology* **8**, 979–987.
19. Vakil, RR and Nilesh, MM 2017. Comparative Study of Bubble Deck Slab and Solid Deck Slab—A Review. International Journal *of Advance Research in* Science *and* Engineering **6**, 383–392.
20. Wilczyński, K, Buziak, K, Wilczyński, KJ, Lewandowski, A and Nastaj, A 2018. Computer Modeling for Single-Screw Extrusion of Wood–Plastic. *Polymer Composites* **10**, 295.
21. Ren, W, Sneed, LH, Yang, Y and He, R 2015. Numerical Simulation of Prestressed Precast Concrete Bridge Deck Panels Using Damage Plasticity Model. *International Journal of Concrete Structures and Materials* **9**, 45–54.

22. Gholamhoseini, A, Gilbert, R, Bradford, M and Chang, Z 2014. Longitudinal shear stress and bond–slip relationships in composite concrete slabs. *Engineering Structures* **69**, 37–48.

23. Bhowmik, R and Mukherjee, S 2018. Evaluation of ductility of RC structures constructed with bubble deck system. *International Journal of Civil Engineering* **16**, 513–526.

24. Clement, T, Ramos, AP, Ruiz, MF and Muttoni, A 2013. Design for punching of prestressed concrete slabs. *Structural Concrete* **14**, 157–167.

25. Sathurappan, G, Rajogopalan, N and Krishnamoorthy, CS 1992. Nonlinear finite element analysis of reinforced and prestressed concrete slabs with reinforcement. *Computers & Structures* **44**, 575–584.

26. Szymczak-Graczyk, A, Garbowski, T and Ksit, B 2024. Influence of geometric parameters on internal forces in the walls of rectangular tanks. *Inżynieria Mineralna*, **1**(2).

27. Garbowski, T, Szymczak-Graczyk, A and Rutkowski J 2024. Optimization of Rectangular Tank Cross-Section Using Trust Region Gradient Method. *Inżynieria Mineralna*, **1**(2).

28. Buannic, N, Cartraud, P and Quesnel, T 2003. Homogenization of corrugated core sandwich panels. *Composite Structures* **59**, 299–312.

29. Xin, L, Khizar, R, Peng, B and Wenbin, Y 2017. Two-Step Homogenization of Textile Composites Using Mechanics of Structure Genome. *Composite Structures* **171**, 252–262.

30. Hohe, J 2003. A direct homogenization approach for determination of the stiffness matrix for microheterogeneous plates with application to sandwich panels. *Composites Part B: Engineering* **34**, 615–626.

31. Biancolini, ME 2005. Evaluation of equivalent stiffness properties of corrugated board. *Composite Structures*, **69**, 322–328.

32. Ramirez-Torres, A, Penta, R, Rodriguez-Ramos, R and Grillo, A 2019. Effective properties of hierarchical fiber-reinforced composites via a three-scale asymptotic homogenization approach. *Mathematics and Mechanics of Solids* **24,** 3554-3574.

33. Garbowski, T and Marek, A 2014. Homogenization of corrugated boards through inverse analysis. In Proceedings of the 1st International Conference on Engineering and Applied Sciences Optimization, Kos Island, Greece, 1751–1766.

34. Garbowski, T and Gajewski, T 2021. Determination of transverse shear stiffness of sandwich panels with a corrugated core by numerical homogenization. *Materials* **14**, 1976.

35. Staszak, N, Garbowski, T and Szymczak-Graczyk, A 2021. Solid Truss to Shell Numerical Homogenization of Prefabricated Composite Slabs. Materials, **14**, 4120.

36. Marek, A and Garbowski, T 2015. Homogenization of sandwich panels. *Computer Assisted Methods in Engineering and Science* **22**, 39–50.

37. Staszak, N, Garbowski, T and Gajewski, T 2023. Optimal Design of Bubble Deck Concrete Slabs: Sensitivity Analysis and Numerical Homogenization. *Materials* **16**, 2320.

38. Gajewski, T, Staszak, N and Garbowski, T 2023. Optimal Design of Bubble Deck Concrete Slabs: Serviceability Limit State. *Materials* **16**, 4897.